Journal of Molecular Liquids xxx (xxxx) 117035

Contents lists available at ScienceDirect

Journal of Molecular Liquids

journal homepage: www.elsevier.com/locate/molliq

Spontaneous formations of nanoconfined water in ionic liquids by small-angle neutron scattering

Hiroshi Abe [a], Fumiya Nemoto [a], Kosuke Hiroi [b], Kazuki Ohishi [c], Shinichi Takata [b]

[a] Department of Materials Science and Engineering, National Defense Academy, Yokosuka 239-8686, Japan
[b] J-PARC Center, Japan Atomic Energy Agency, Tokai, Ibaraki 319-1195, Japan
[c] Research Center for Neutron Science and Technology, Comprehensive Research Organization for Science and Society (CROSS), Tokai, Ibaraki 319-1106, Japan

ARTICLE INFO

Article history:
Received 26 May 2021
Received in revised form 13 July 2021
Accepted 15 July 2021

Keywords:
Water pocket
Ionic liquids
Alkyl chain length dependence
Small-angle neutron scattering

ABSTRACT

In this study, monodispersive nanoconfined water ("water pocket") is organized spontaneously in hydrophilic ionic liquid (IL). The IL is 1-alkyl-3-methylimidazolium nitrate ($[C_n mim][NO_3]$ n = 2, 6, and 8). By small-angle neutron scattering (SANS), D_2O aggregations in the IL are detected. There are no SANS peaks for $[C_2mim][NO_3]$–D_2O, but, in $[C_6mim][NO_3]$–x mol% D_2O, a SANS peak can be observed at $70 < x < 90$ mol%. The peak intensity, position, and profile change according to water concentration and temperature. Pure $[C_8mim][NO_3]$ has a distinct SANS peak, reflecting on the nanodomains at room temperature. Above 70 mol%, the SANS peak of $[C_8mim][NO_3]$–D_2O sharply increases and shifts to the low-Q position. The water pocket develops proportionate to water concentration, and its morphologies are visualized using an ab initio bead model. The alkyl chain length dependence of the water pocket is clarified by a three-dimensional reconstruction method.

1. Introduction

The nanoconfinement of water has been widely investigated to identify differences with respect to the bulk water. The properties of nanoconfined water have been clarified using size-tunable mesoporous silica materials [1]. Melting points on the pore-size scale indicate the size effect of the hydrogen bonding network. Moreover, three water types have been classified via Raman spectroscopy and attenuated total reflectance Fourier transform (FT) infrared spectrometry. The two-dimensional confinement of water has been conducted using graphene [2,3]. With water sandwiched by graphene sheets, molecular dynamic (MD) simulations demonstrated the phase transitions and thus phase diagram [2]. The one-dimensional (1D) behavior of the nanoconfined water inside carbon nanotubes has been examined by Raman spectroscopy [4] and AC impedance [5], the results of which suggest that diameter influences fluid phase transitions. Moreover, 1D channeling of high proton conduction was induced in the hydrophobic metal–organic nanotube [5].

Ionic liquid (IL) has been utilized as a novel solvent in various research fields [6–11]. IL is designed and synthesized freely by a combination of cations and anions. Nanoheterogeneity in the liquid state has been demonstrated by MD as a characteristic feature of IL [12]; the IL was 1-alkyl-3-methylimidazolium hexafluorophosphate ($[C_n mim][PF_6]$ (n = 2, 4, 6, and 8), where n is the alkyl chain length). With increasing n, polar and nonpolar nanodomains developed in the simulation box. Experimentally, the nanoheterogeneity of $[C_n mim][Cl]$ (n = 3, 4, 6, 8, and 10) was detected by small- and wide-angle X-ray scattering (SWAXS) [13]. A prepeak appeared at the low–Q of the SWAXS patterns, the intensity and position of which changed according to n. In both pure and mixed systems, nanoheterogeneous liquid structures have been investigated as the fourth evolution of IL [14]. For instance, the nanoconfined water in $[C_8mim][NO_3]$ has been simulated by MD [15]; the nanoconfined water existed near the nanodomain boundaries. Another MD simulation [16] suggested that $[C_4mim]^+$ cations are repulsive to water; thus, water can be excluded from polar nanodomains. Using small-angle X-ray scattering and small-angle neutron scattering (SANS), the hidden information of neutron-enhanced D_2O aggregation in $[C_4mim][NO_3]$ has been extracted, where the monodispersive nanoconfined water in the IL was referred to as a "water pocket" [17,18]. The water pocket formed spontaneously in the water-rich region ($70 < x < 90$ mol% D_2O) and can explain the partial refolding of protein [19]. Moreover, via simultaneous wide-angle X-ray scattering (WAXS) and differential scanning calorimetry (DSC), the water pocket at the specific water–concentration region prevented crystal nucleation of both IL and ice at low temperatures [20]. Furthermore, the slow dynamics of the water pocket were clarified by quasielastic neutron scattering, the results of which were compared with bulk water [21]. The peculiar features of the water pocket have been summarized by [22,23].

https://doi.org/10.1016/j.molliq.2021.117035
0167-7322/

In this study, we investigate the alkyl chain length dependence of $[C_n\text{mim}]^+$ (n = 2, 6, and 8) cations for the water pocket using SANS. By changing the water concentration and temperature, the size, shape, and distribution of the water pocket in the IL are estimated by examining the SANS peak.

2. Experiments

2.1. Materials

$[C_2\text{mim}][NO_3]$, which is in a solid state at room temperature, was purchased from Tokyo Chemical Industry, Co. (>98.0%). $[C_6\text{mim}][NO_3]$ and $[C_8\text{mim}][NO_3]$ were purchased from Angene Chemical, Co. (>98.0%). We used the as-received samples without vacuum drying at 373 K for a few days. Table 1 lists the densities of $[C_2\text{mim}][NO_3]$ [24], $[C_4\text{mim}][NO_3]$ [25], $[C_6\text{mim}][NO_3]$ [26], and $[C_8\text{mim}][NO_3]$ [27]. Considering neutron scattering length density (SLD), distilled D_2O (99.9%, Merck Co.) was selected as an additive to enhance the water pocket. The mixture of hydrophilic IL and D_2O was prepared inside a glove box under flowing helium gas to avoid atmospheric moisture. The SLD values of $[C_n\text{mim}]^+$ cations are relatively small (Table 1). Thus, $[NO_3]^-$ and D_2O are observable in the SANS.

2.2. Simultaneous measurement of wide-angle X-ray scattering and differential scanning calorimetry

To clarify the complicated phase behaviors, a DSC instrument was attached to the X-ray diffractometer [28]. Simultaneous WAXS and DSC measurements were conducted (SmartLab, Rigaku Co.) using Cu Kα radiation (λ = 1.542 Å). A 1D detector (D/tex, Rigaku Co.) was used for fast scanning (θ-2θ scan). DSC windows for WAXS were metal-coated Mylar films. The temperature range for the simultaneous measurements was 293–173 K. The cooling/heating rate was 5 K/min. During the simultaneous measurements, dry nitrogen gas was flowing at 20 mL/min to reduce moisture.

2.3. Small-angle neutron scattering

SANS experiments were conducted on the BL15 (TAIKAN) at the Japan Proton Accelerator Research Complex (J-PARC) [29]. To observe a hierarchical structure on the wide Q-range, small-, medium-, and high-angle detector banks have been equipped on the TAIKAN. Here, the scattering vector Q was defined as $4\pi(\sin\theta)/\lambda$ ($Å^{-1}$), where the scattered angle was 2θ. A sample changer was mounted onto the goniometer. Temperature was controlled with a circulating bath (Ministat 125, Huber, Co.) The mixtures were inserted into a quartz cell (thickness of 1.0 mm; Starna Scientific Ltd.) with a low neutron absorption ability. We analyzed the observed data quantitatively using background intensities, e. g., empty-cell, glassy carbon, and D_2O-filled-cell scattering. In the data analysis, we used the scattering data with 2–5 Å. It is well known that samples containing a large amount of hydrogen provide modified profiles above 1.5 $Å^{-1}$ [29]. The data reduction was tuned by changing the incident wavelength regions.

Table 1
Density of $[C_n\text{mim}][NO_3]$ (n = 4, 6, and 8) and neutron SLD of $[C_n\text{mim}]^+$ (n = 4, 6, and 8) cations, $[NO_3]^-$ anion, and D_2O.

	$[C_2\text{mim}][NO_3]$ [24]	$[C_4\text{mim}][NO_3]$ [25]	$[C_6\text{mim}][NO_3]$ [26]	$[C_8\text{mim}][NO_3]$ [27]		
Density (g/cm^3)	1.209	1.160	1.190	1.074		
		293 K	293 K			
	$[C_2\text{mim}]^+$	$[C_4\text{mim}]^+$	$[C_6\text{mim}]^+$	$[C_8\text{mim}]^+$	$[NO_3]^-$	D_2O
SLD ($\times 10^{-6}$ [$Å^{-2}$])	0.618	0.427	0.298	0.219	1.57	6.37

3. Results and discussion

3.1. Small-angle neutron scattering of $[C_2mim][NO_3]$–D_2O

$[C_2\text{mim}][NO_3]$ is in a solid state at room temperature, and it crystallizes simply on cooling at ambient pressure, whereas the complicated crystal polymorph and multiple crystallization pathways are induced under high pressure [30]. Fig. 1 shows the low-Q intensities of $[C_2\text{mim}][NO_3]$–x mol% D_2O at room temperature, from which it is evident that no distinct prepeaks exist over the whole water concentration. Moreover, the background intensities decreased with an increase in D_2O concentration, since the incoherent scattering of H atoms of the $[C_2\text{mim}]^+$ cation was reduced. Therefore, the water pocket for $[C_4\text{mim}][NO_3]$–D_2O observed by [17] was not formed in $[C_2\text{mim}][NO_3]$–x mol% D_2O at room temperature. This result is consistent with the little nanoheterogeneity of pure $[C_2\text{mim}][NO_3]$. The little nanoheterogeneity and lack of a water pocket support the idea that the water pocket can only be organized by the distinct nanoheterogeneity of the IL. We predict that each water molecule is isolated because of the weak nanoheterogeneity of $[C_2\text{mim}][NO_3]$. A principal peak tail was observed at approximately 1.6 $Å^{-1}$ (Q_2). The observed intensities can mainly be derived from the weak correlation between $[NO_3]^-$ and D_2O because of the small SLD value of $[C_2\text{mim}]^+$ (Table 1). Even at 280 K, the water concentration dependence of the SANS profile does not change. Thus, the water pocket cannot exist in $[C_2\text{mim}][NO_3]$ media.

3.2. Small-angle neutron scattering of $[C_6mim][NO_3]$–D_2O

Pure $[C_6\text{mim}][NO_3]$ did not crystallize at low temperatures. A glass transition was observed by the simultaneous WAXS and DSC measurements (Fig. S1). Since pure $[C_6\text{mim}][NO_3]$ is in a liquid state at room temperature, a weak and broad prepeak in the pure system can be was observed at 0.3–0.4 $Å^{-1}$ (Q_1) in Fig. 2(a). A principal peak can be observed in the vicinity of Q_2. In the mixed system, a distinct peak at Q_1 appears with an increase in water concentration, and the Q_1 peak shifts to the low-Q position. Particularly, the Q_1 peak becomes sharp accompanied by an increasing peak intensity at 70–90 mol% D_2O (Fig. 2(a)). This implies that the water pocket inside $[C_6\text{mim}][NO_3]$ formed in the same manner as in $[C_4\text{mim}][NO_3]$–D_2O [17]. The average size of the water pocket in $[C_6\text{mim}][NO_3]$–D_2O was 20–25 Å, which is comparable to that in $[C_4\text{mim}][NO_3]$–D_2O. At 95 mol%, the water pocket in

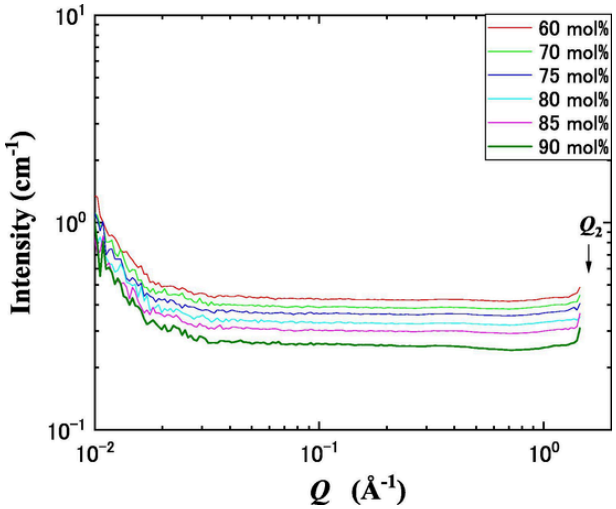

Fig. 1. SANS of $[C_2\text{mim}][NO_3]$–x mol% D_2O at 298 K (x = 60, 70, 75, 80, 85, and 90).

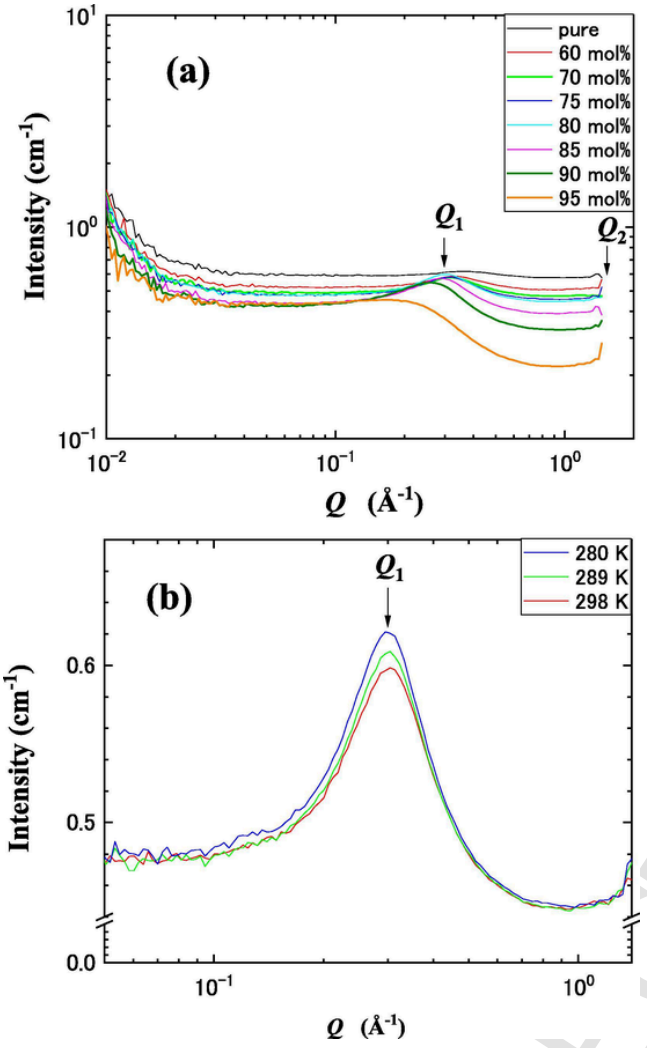

Fig. 2. SANS of (a) water concentration dependence [C_6mim][NO_3]–x mol% D_2O at 298 K, and (b) temperature dependence of SANS peak in [C_6mim][NO_3] –80 mol% D_2O.

[C_6mim][NO_3] almost collapsed, judging from the absence of the Q_1 peak. We deduce that the water additive might percolate over the whole region, and the IL can be confined inversely above 95 mol%.

Generally, the water pocket, which is loosely packed in the IL, is influenced by the thermal fluctuation of IL host nanodomains. For instance, the water pocket in [C_4mim][NO_3] developed at low temperatures [18]. Here, we focus on [C_6mim][NO_3]–80 mol% D_2O, since the water pocket is stable at $70 < x < 90$ mol%. Fig. 2(b) reveals the temperature dependence of the representative Q_1 peak of [C_6mim][NO_3] –80 mol% D_2O, from which it is evident that the Q_1 peak is asymmetric at 298 K. With a decrease in temperature, the SANS intensity at Q_1 increased slightly and shifted to the low-Q region accompanied by peak broadening. The peak broadening at 280 K implies that water pocket coarsening occurred at low temperatures. For quantitative estimation, we introduced the intensity change provided by $\Delta I/I$ (%), where $\Delta I = I$ (280 K) - I(298 K). The $\Delta I/I$ of [C_6mim][NO_3]–80 mol% D_2O is larger than that of [C_4mim][NO_3]–80 mol% D_2O (Table 2).

3.3. Small-angle neutron scattering of [C_8mim][NO_3]–D_2O

The glass transition of pure [C_8mim][NO_3] was detected at low temperatures using simultaneous WAXS and DSC measurements (Fig. S2). The glass transition temperature (T_g) was estimated to be 201 K. Upon heating, liquid crystal and crystal phases did not appear, even though

Table 2
Q_1 peak intensity, position, width, $\Delta I/I$, and shape of [$C_n$mim][NO_3]–80 mol% D_2O (n = 2, 4, 6, and 8).

	Intensity	position (Å^{-1})	width (Å^{-1})	$\Delta I/I$ (%)	shape
n = 2	no	–	–	–	–
n = 4	weak	0.33	0.44	2.3	trapezoid
n = 6	medium	0.30	0.20	17.4	asymmetric
n = 8	strong	0.25	0.070	15.7	symmetric

phase transitions of [C_8mim][NO_3] were predicted by MD simulations [32]. At room temperature, pure [C_8mim][NO_3] exists in the liquid state. Fig. 3(a) shows the SANS profile of pure [C_8mim][NO_3] at 298 K. In contrast to pure [C_6mim][NO_3], the prepeak at Q_2 of pure [C_8mim][NO_3] is more distinct, which implies that nanodomains in the pure system became larger and nanoheterogeneity developed over the medium range. The small SLD value of [C_8mim]$^+$ in Table 1 suggests that [NO_3]$^-$ aggregations contribute mainly to the sharp prepeak of pure [C_8mim][NO_3]. By adding water, the prepeak shifted and increased drastically above 70 mol%. Compared with [C_6mim][NO_3]–D_2O, the Q_1 peak of [C_8mim][NO_3]–D_2O became much larger, which suggests that the water pocket has a high population and long lifetime. Proportional to the alkyl chain length of the cations, the sufficiently large water pocket was very stable inside the larger nanodomains of [C_8mim][NO_3]. At 95 mol% as the percolation limit of [C_4mim][NO_3]–D_2O [17], the peak profile drastically changes: the prepeak spreads widely in the center of 0.19 Å^{-1}. This implies that polydispersive fluctuations can be realized in [C_8mim][NO_3]–95 mol% D_2O. Moreover, the size of the water pocket can be tuned by the alkyl chain length of the [$C_n$mim]$^+$ cations.

Our next step is to estimate flexibility of the nanoconfinement flexibility and softness/hardness of the water pocket from the thermal properties of [C_8mim][NO_3]–D_2O. The temperature dependence of the SANS peak at Q_1 is almost the same at $70 < x < 90$ mol%. The Q_1 peak in [C_8mim][NO_3]–80 mol% D_2O is indicated in Fig. 3(b), from which it is evident that the increment of the Q_1 peak intensity is large upon cooling and comparable with the $\Delta I/I$ of [C_6mim][NO_3]–80 mol% D_2O (Table 2). Hence, the water pockets in [C_6mim][NO_3] and [C_8mim][NO_3] develop further at low temperatures. Generally, diffraction theory indicates that the Debye–Waller factor containing elastic constants as a thermal effect influences the scattered intensity [33]. Thus, a large $\Delta I/I$ of [C_6mim][NO_3]–80 mol% D_2O and [C_8mim][NO_3]–80 mol% D_2O was derived from the softness of the water pocket.

To interpret the low-temperature behavior of the water pocket in [C_8mim][NO_3], we examine the nanoheterogeneity of pure [C_8mim][NO_3]. Fig. 3(c) depicts the temperature dependence of the Q_1 peak in pure [C_8mim][NO_3]; a distinct prepeak was only observed in SANS for pure [C_8mim][NO_3]. With respect to the temperature dependence of the peak intensity, the $\Delta I/I$ of pure [C_8mim][NO_3] is almost equivalent to that of [C_8mim][NO_3]–80 mol% D_2O. Therefore, the softness of the water pocket is influenced by the softness of the nanodomains in the IL. The sharp prepeak of pure [C_8mim][NO_3] at 298 K broadened and shifted to the low-Q position at low temperatures, where 280 K is greater than T_g. This result is consistent with the temperature dependence of a prepeak in pure [C_8mim][BF_4] by SWAXS [13]. It is well known that the hydrophobic tail of [$C_n$mim]$^+$ cations causes the formation of a nonpolar nanodomain, which has fast dynamics [34]. Since the nonpolar nanodomain is described by a markedly low thermal activation, the prepeak intensity by SWAXS increased by developing nanoheterogeneity upon cooling. It should be noted that in the SANS experiment, the nonpolar nanodomain of [C_8mim]$^+$ does not exist because of the small SLD (Table 1). By contrast, the SLD of [NO_3]$^-$ is sufficiently large in the SANS. We predict that the Q_1 peak in pure [C_8mim][NO_3] (Fig. 3(c)) originates from the polar nanodomains derived from [NO_3]$^-$ aggregates. Hence, in a pure system, a supercooled

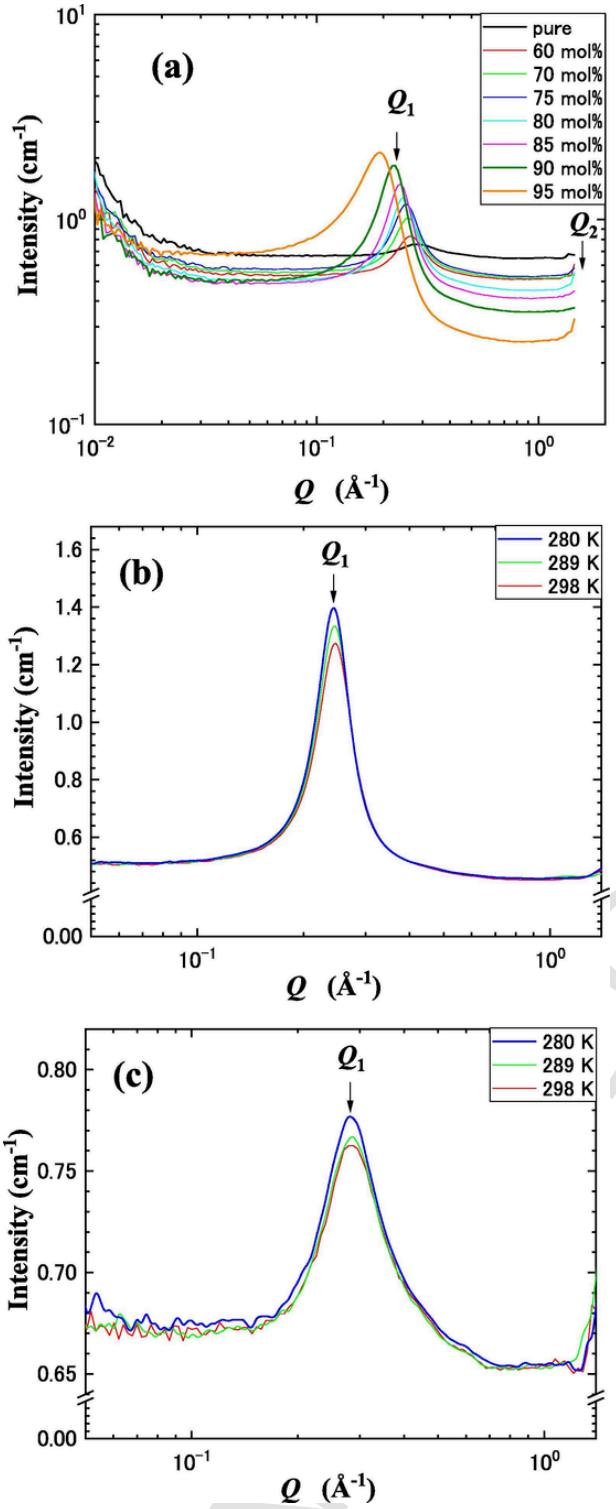

Fig. 3. SANS of (a) water concentration dependence $[C_8mim][NO_3]$–x mol% D_2O at 298 K, (b) temperature dependence of SANS peak in $[C_8mim][NO_3]$ –80 mol% D_2O, and (c) temperature dependence of SANS peak in pure $[C_8mim][NO_3]$.

liquid state at low temperatures described by the broad prepeak can be explained by $[NO_3]^-$ aggregations.

Combined with the temperature dependence of the Q_1 peak intensity in the pure system, a loosely packed and soft water pocket of $[C_8mim][NO_3]$–80 mol% D_2O grew at low temperatures, accompanied by $[NO_3]^-$ aggregates. Here, we confirm that a large and soft water pocket is promoted in $[C_8mim][NO_3]$. Considering the Q_1 peak position, peak width, and $\Delta I/I$ in Table 2, we can tune the softness and size of the water pocket by selecting $[C_nmim]^+$ cations.

3.4. Ab initio bead modeling of the water pocket

Small-angle scattering (SAS) can be interpreted using various models. Model-free analysis has been developed by introducing indirect FT [35]. The pair-distance distribution function, $P(r)$, represents the intra- and inter-particle interactions. The observed SAS was smoothly fitted by the indirect FT method, and $P(r)$ was estimated simultaneously using the *GNOM* [35] in the *ATSAS* software package. Density fluctuations obtained by SAS are expressed in size, shape, and distribution. To visualize the arbitrary shapes of the density fluctuations in real space, a low-resolution *ab initio* shape determination method has been developed for biomolecules in the aqueous solution. The *ab initio* reconstruction simulation programs for various shape and formation types of protein structures are unified in the *ATSAS* software package [36–39].

In $[C_6mim][NO_3]$–D_2O, a distinct Q_1 peak can be observed at $70 < x < 90$ mol%. The peak sharpens and shifts from 70 to 90 mol%, which corresponds to the variable formations of the water pocket. To visualize the variable formations on the water concentration scale, we simulated the size, shape, and distribution of the water pocket using *ATSAS* software package. At first, the observed SANS data of $[C_6mim][NO_3]$–D_2O and $[C_8mim][NO_3]$–D_2O were analyzed using *GNOM* after absolute value correction. *GNOM* can optimize $P(r)$ by referring to the observed SANS profile. Fig. 4(a) shows the fitted SANS profile of $[C_6mim][NO_3]$–80 mol% D_2O at 298 K, as an example, where the observed SANS intensity is represented by red closed circles and the calculated SANS intensity is represented by the gray curve. The calculated intensity is consistent with the observed asymmetric profile. At the same time, $P(r)$ was obtained by using the boundary condition of $P(r) = 0$ at $r \to 0$ and $r \to r_{max}$. Fig. 4(b) shows the $P(r)$ of $[C_6mim][NO_3]$ –80 mol% D_2O at 298 K. The $P(r)$ oscillation of $[C_6mim][NO_3]$–D_2O is dominant compared with that of $[C_4mim][NO_3]$–D_2O [17]: the oscillation of $[C_4mim][NO_3]$–D_2O decays rapidly, whereas the oscillation of

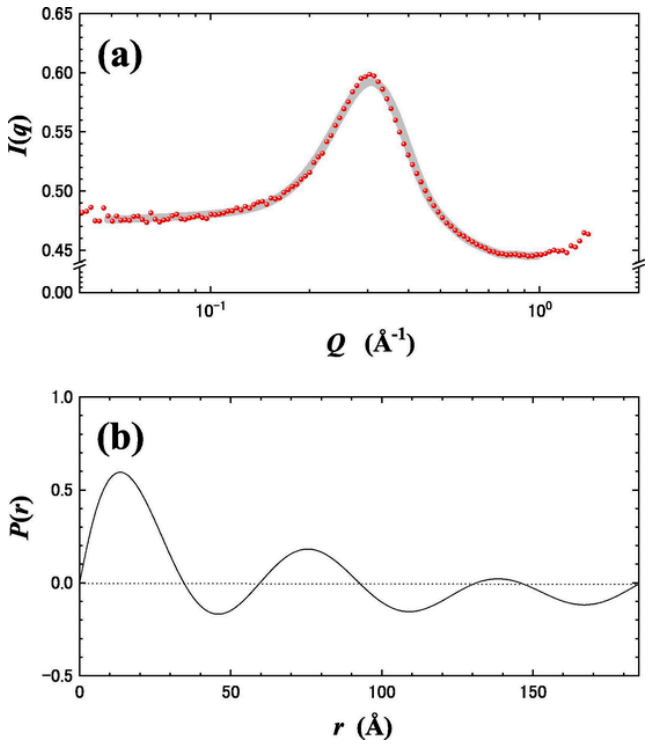

Fig. 4. (a) Observed and calculated SANS intensities of $[C_6mim][NO_3]$ –80 mol% D_2O at 298 K and (b) $P(r)$.

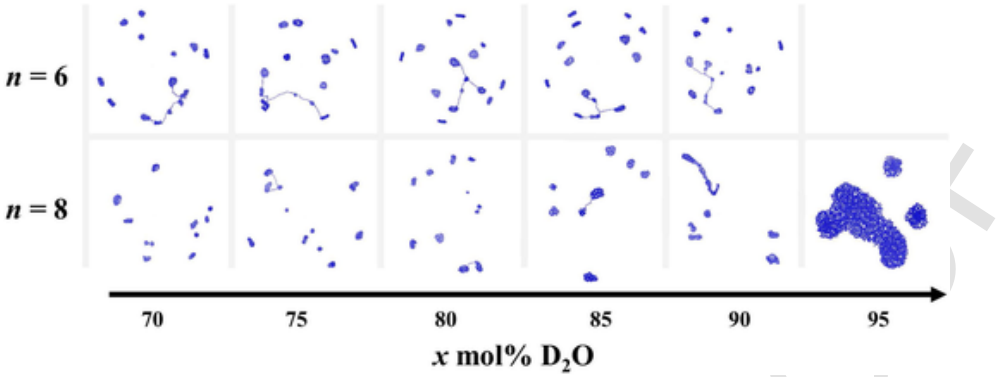

Fig. 5. *Ab initio* simulation results of $[C_6mim][NO_3]$–D_2O and $[C_8mim][NO_3]$–D_2O with respect to the SANS peak and $P(r)$ at 298 K. $[C_nmim]^+$ cations and $[NO_3]^-$ anion are omitted.

$[C_6mim][NO_3]$–D_2O has a long period. The large oscillating $P(r)$ for $[C_6mim][NO_3]$–D_2O implies that the correlation strength among water pockets is large. The longer tail of the $[C_6mim]^+$ cations excludes water molecules from the hydrophobic nonpolar nanodomain and thereby promotes the water pocket formation.

Three-dimensional model reconstruction in real space using SAS data is a recent trend to explain the structure and property of proteins in a solution. The nanostructure shape is represented by a dummy bead assembly. We have already shown the visualization of the monodispersive water pocket in $[C_4mim][NO_3]$–D_2O [17,18] using the *GASBOR* [36] program in *ATSAS* [36–39]. The shape and distribution of the water pocket using *ab initio* modeling are similar to those obtained by MD simulations [15]. Fig. 5 shows the morphologies of the water pocket in $[C_6mim][NO_3]$ and $[C_8mim][NO_3]$ at 298 K. The aggregation shape in real space was approximately reconstructed with dummy beads in the simulation box. The reconstruction is a snapshot in real time and space of the water pockets, which are obtained from the SANS peak. In $[C_6mim][NO_3]$–x mol% D_2O, the monodispersive water pockets are well demonstrated and characterized by anisotropic shapes. With an increase in water concentration, the size of the water pocket in $[C_6mim][NO_3]$–D_2O changes slightly. More interestingly, some water pocks are linked with others by a water string. The water bridging expressed by the water string is seen at $70 < x < 90$ mol%. Since the water bridging is also simulated in $[C_4mim][NO_3]$–D_2O with a trapezoid peak shape [17], the asymmetric peak profile of $[C_6mim][NO_3]$–D_2O provides the water bridging. *GASBOR* was originally improved to find a chain-like distribution [40]. In fact, it is reconstructed that two globular domains are connected by a linker using *GASBOR* [41]. By changing temperature, the domain structural transformation from a single globular domain to two globular domains was demonstrated, where $P(r)$ was calculated from the scattering data at 0.02 and 0.28 $Å^{-1}$.

In contrast to the slight water concentration dependence of $[C_6mim][NO_3]$–D_2O, a water pocket with intense water consecration dependency was obtained in $[C_8mim][NO_3]$–D_2O, and it coarsened with an increase in water concentration. However, at 95 mol%, water occupies mainly in space, and their sizes become polydispersive. The simulated 95 mol% mixture resembled the MD simulation result of $[C_8mim][NO_3]$–95.2 mol% water [15]. Consequently, the monodispersive water pocket vanished at 95 mol%, and a water-dominant state was transferred between 90 and 95 mol%. Focusing on the water bridging in Fig. 5, in $[C_8mim][NO_3]$–D_2O, rare water bridging was simulated for some water concentrations, which is related to the symmetric SANS profile of $[C_8mim][NO_3]$–D_2O. Hence, nonsymmetric SANS peak profile corresponds to the inherent water bridging among water pockets.

4. Conclusions

Monodispersive nanoconfined water ("water pocket") was organized spontaneously in the hydrophilic IL $[C_nmim][NO_3]$ (n = 4, 6, and 8), and the relationship of the water pocket with the nanoheterogeneity of IL was examined by SANS experiments. Q_1 peak enhancement in the water-rich region was caused by the water pocket. The water pocket size varied extensively according to the alkyl chain length of the $[C_nmim]^+$ cations. Particularly for $[C_8mim][NO_3]$–x mol% D_2O, a large water pocket formed. At 95 mol%, the water pocket collapsed, resulting in large and polydispersive water fluctuations. By the temperature dependence of the SANS intensities, the softness/hardness of the water pocket was evaluated qualitatively. A soft water pocket was realized in $[C_6mim][NO_3]$ and $[C_8mim][NO_3]$ with flexible nanodomains. The size, shape, and distribution of the water pocket were demonstrated using the *ab initio* bead model. Size, softness/hardness, and distribution of the water pocket can be tuned by water concentration, temperature, and alkyl chain length of the $[C_nmim]^+$ cation. The water pocket proposed in this paper is a promising technique for next-generation nanoheterogeneity engineering.

Uncited reference

[31].

CRediT authorship contribution statement

Hiroshi Abe: Conceptualization, Writing – original draft, Writing – review & editing. **Fumiya Nemoto:** Data curation, Formal analysis. **Kosuke Hiroi:** Data curation, Formal analysis. **Kazuki Ohishi:** Data curation. **Shinichi Takata:** Formal analysis.

Declaration of Competing Interest

The authors declare that they have no known competing financial interests or personal relationships that could have appeared to influence the work reported in this paper.

Acknowledgments

We thank Dr. T. Takekiyo and Professor Y. Yoshimura of the National Defense Academy and Professor A. Shimizu of Soka University for helpful discussions. We acknowledge the support of J-PARC; activity under the "Size effect of nano-confined water in ionic liquids" program (Proposal No. 2020B0018).

Appendix A. Supplementary material

Supplementary data to this article can be found online at https://doi.org/10.1016/j.molliq.2021.117035.

References

[1] A.W. Knight, N.G. Kalugin, E. Coker, A.G. Ilgen, Water properties under nano-scale confinement, Sci. Rep. 9 (2019) 8246–8312.
[2] Z. Gao, N. Giovambattista, O. Sahin, Phase Diagram of Water Confined by Graphene, Sci. Rep. 8 (2018) 6228–6311.
[3] F. Jiménez-Ángeles, K.J. Harmon, T. Dac Nguyen, P. Fenter, M.O. de la Cruz, Nonreciprocal interactions induced by water in confinement, Phys. Rev. Res. 2 (2020) 043244–043318.
[4] K.V. Agrawal, S. Shimizu, L.W. Drahushuk, D. Kilcoyne, M.S. Strano, Observation of extreme phase transition temperatures of water confined inside isolated carbon nanotubes, Nat. Nanotech. 12 (3) (2017) 267–273.
[5] K. Otake, K. Otsubo, T. Komatsu, S. Dekura, J.M. Taylor, R. Ikeda, K. Sugimoto, A. Fujiwara, C.-P. Chou, A.W. Sakti, Y. Nishimura, H. Nakai, H. Kitagawa, Confined water-mediated high proton conduction in hydrophobic channel of a synthetic nanotube, Nat. Commun. 11 (2020) 843–847.
[6] T. Welton, Room-Temperature Ionic Liquids. Solvents for Synthesis and Catalysis, Chem. Rev. 99 (8) (1999) 2071–2084.
[7] L.A. Blanchard, D. Hancu, E.J. Beckman, J.F. Brennecke, Green processing using ionic liquids and CO_2, Nature 399 (6731) (1999) 28–29.
[8] R.P. Swatloski, S.K. Spear, J.D. Holbrey, R.D. Rogers, Dissolution of Cellose with Ionic Liquids, J. Am. Chem. Soc. 124 (18) (2002) 4974–4975.
[9] M. Armand, F. Endres, D.R. MacFarlane, H. Ohno, B. Scrosati, Ionic-liquid materials for the electrochemical challenges of the future, Nature Mater. 8 (8) (2009) 621–629.
[10] Z. Lei, B. Chen, Y.-M. Koo, D.R. MacFarlane, Introduction: Ionic Liquids, Chem. Rev. 117 (2017) 6633–6635.
[11] M. Watanabe, M.L. Thomas, S. Zhang, K. Ueno, T. Yasuda, K. Dokko, Application of Ionic Liquids to Energy Storage and Conversion Materials and Devices, Chem. Rev. 117 (2017) 7190–7239.
[12] J.N.A. Canongia Lopes, A.A.H. Pádua, Nanostructural Organization in Ionic Liquids, J. Phys. Chem. B 110 (7) (2006) 3330–3335.
[13] A. Triolo, O. Russina, H.-J. Bleif, E. Di Cola, Nanoscale Segregation in room temperature ionic liquids, J. Phys. Chem. B 111 (18) (2007) 4641–4644.
[14] D.R. MacFarlane, A.L. Chong, M. Forsyth, M. Kar, R. Vijayaraghavan, A. Somers, J. M. Pringle, New dimensions in salt–solvent mixtures: a 4th evolution of ionic liquids, Faraday Discuss. 206 (2018) 9–28.
[15] W. Jiang, Y. Wang, G.A. Voth, Molecular dynamics simulation of nanostructural organization in ionic liquid/water mixtures, J. Phys. Chem. B 111 (2007) 4812–4818.
[16] C. Schröder, T. Rudas, G. Neumayr, S. Benkner, O. Steinhauser, On the collective network of ionic liquid/water mixtures. I. Orientational structure, J. Chem. Phys. 127 (23) (2007) 234503, https://doi.org/10.1063/1.2805074.
[17] H. Abe, T. Takekiyo, M. Shigemi, Y. Yoshimura, S. Tsuge, T. Hanasaki, K. Ohishi, S. Takata, J. Suzuki, Direct Evidence of Confined Water in Room-Temperature Ionic Liquids by Complementary Use of Small-Angle X-ray and Neutron Scattering, J. Phys. Chem. Lett. 5 (2014) 1175–1180.
[18] H. Abe, T. Takekiyo, M. Shigemi, Y. Yoshimura, S. Tsuge, T. Hanasaki, K. Ohishi, S. Takata, J. Suzuki, Size-tunable Confined Water in a Room Temperature Ionic Liquid, JPS Conf. Proc. 8 (2015) 033001–033006.
[19] T. Takekiyo, K. Yamazaki, E. Yamaguchi, H. Abe, Y. Yoshimura, High Ionic Liquid Concentration-Induced Structural Change of Protein in Aqueous Solution: A Case Study of Lysozyme, J. Phys. Chem. B 116 (36) (2012) 11092–11097.
[20] H. Abe, T. Takekiyo, Y. Yoshimura, K. Saihara, A. Shimizu, Anomalous Freezing of Nano-Confined Water in Room-Temperature Ionic Liquid 1-Butyl-3-Methylimidazolium Nitrate, ChemPhysChem 17 (8) (2016) 1136–1142.
[21] H. Abe, T. Yamada, K. Shibata, Dynamic properties of nano-confined water in an ionic liquid, J. Mol. Liq. 264 (2018) 54–57.
[22] H. Abe, T. Takekiyo, Y. Yoshimura, A. Shimizu, Static and dynamic properties of nano-confined water in room-temperature ionic liquids, J. Mol. Liq. 290 (2019) 111216–111219.
[23] H. Abe, Phase variety in ionic liquids: Hydrogen bonding and molecular conformations, J. Mol. Liq. 332 (2021) 115189–115227.
[24] F.Y. Zhao, L.Y. Liang, J.Y. Wang, Y.Q. Hu, Density and surface tension of binary mixtures of 1-ethyl-3-methylimdazolium nitrate with alcohols, Chinese Chem. Lett. 23 (11) (2012) 1295–1298.
[25] B. Mokhtarani, A. Sharifi, H.R. Mortaheb, M. Mirzaei, M. Mafi, F. Sadeghian, Density and viscosity of 1-butyl-3-methylimidazolium nitrate with ethanol, 1-propanol, or 1-butanol at several temperatures, J. Chem. Thermodyn. 41 (12) (2009) 1432–1438.
[26] Z. Khedri, M. Almasi, A. Maleki, Thermodynamic Properties of 1-Hexyl-3-methylimidazolium Nitrate and 1-Alkanols Mixtures: PC-SAFT Model, J. Chem. Eng. Data 64 (10) (2019) 4465–4473.
[27] B. Mokhtarani, A. Sharifi, H.R. Mortaheb, M. Mirzaei, M. Mafi, F. Sadeghian, Densities and Viscosities of Pure 1-Methyl-3-octylimidazolium Nitrate and Its Binary Mixtures with Alcohols at Several Temperatures, J. Chem. Eng. Data 55 (9) (2010) 3901–3908.
[28] T. Arii, A. Kishi, Y. Kobayashi, A new simultaneous apparatus for X-ray diffractometry and differential scanning calorimetry (XRD-DSC), Thermochim Acta 325 (2) (1999) 151–156.
[29] S. Takata, J. Suzuki, T. Shinohara, T. Oku, T. Tominaga1, K. Ohishi, H. Iwase, T. Nakatani, Y. Inamura, T. Ito, K. Suzuya, K. Aizawa, M. Arai, T. Otomo, M. Sugiyama, The Design and q Resolution of the Small and Wide Angle Neutron Scattering Instrument (TAIKAN) in J-PARC, JPS Conf. Proc. 8 (2015) 036020-6.
[30] H. Abe, T. Takekiyo, Y. Yoshimura, N. Hamaya, S. Ozawa, Crystal Polymorphs and Multiple Crystallization Pathways of Highly Pressurized 1-Ethyl-3-Methylimidazolium Nitrate, Aust. J. Chem. 72 (2) (2019) 87, https://doi.org/10.1071/CH18368.
[31] C.E.S. Bernardes, K. Shimizu, A.I.M.C. Lobo Ferreira, L.M.N.B.F. Santos, J.N. Canongia Lopes, Structure and Aggregation in the 1,3-Dialkyl-imidazolium Bis (trifluoromethylsulfonyl)imide Ionic Liquid Family: 2. From Single to Double Long Alkyl Side Chains, J. Phys. Chem. B 118 (2014) 6885–6895.
[32] W. Cao, Y. Wang, G. Saielli, Metastable State during Melting and Solid-Solid Phase Transition of $[C_n\text{Mim}][NO_3]$ (n = 4–12) Ionic Liquids by Molecular Dynamics Simulation, J. Phys. Chem. B 122 (1) (2018) 229–239.
[33] B.E. Warren, X-Ray Diffraction, Dover, 1990.
[34] Y.-L. Wang, B. Li, S. Sarman, F. Mocci, Z.-Y. Lu, J. Yuan, A. Laaksonen, M.D. Fayer, Microstructural and Dynamical Heterogeneities in Ionic Liquids, Chem. Rev. 120 (2020) 5798–5877.
[35] D.I. Svergun, Determination of the regularization parameter in indirect-transform methods using perceptual criteria, J. Appl. Cryst. 25 (4) (1992) 495–503.
[36] D.I. Svergun, M.V. Petoukhov, M.H.J. Koch, Determination of domain structure of proteins from X-ray solution scattering, Biophys. J . 80 (6) (2001) 2946–2953.
[37] P.V. Konarev, M.V. Petoukhov, V.V. Volkov, D.I. Svergun, ATSAS 2.1, a program package for small-angle scattering data analysis, J. Appl. Cryst. 39 (2) (2006) 277–286.
[38] M.V. Petoukhov, P.V. Konarev, A.G. Kikhney, D.I. Svergun, ATSAS 2.1 - towards automated and web-supported small-angle scattering data analysis, J. Appl. Cryst. 40 (s1) (2007) s223–s228.
[39] M.V. Petoukhov, D. Franke, A.V. Shkumatov, G. Tria, A.G. Kikhney, M. Gajda, C. Gorba, H.D.T. Mertens, P.V. Konarev, D.I. Svergun, New developments in the ATSAS program package for small-angle scattering data analysis, J. Appl. Cryst. 45 (2) (2012) 342–350.
[40] M.V. Petoukhov, D.I. Svergun, New methods for domain structure determination of proteins from solution scattering data, J. Appl. Cryst. 36 (3) (2003) 540–544.
[41] A. Di Poto, M. Papi, S. Trivedi, A. Maiorana, P. Gavazzo, M. Vassalli, F.D. Lowy, M. De Spirito, L. Montanaro, M. Imbriani, C.R. Arciola, L. Visai, In vitro effect of temperature on the conformational structure and collagen binding of SdrF, a *Staphylococcus epidermidis* adhesin, Appl. Microbio. Biotech. 99 (13) (2015) 5593–5603.